

# Fusion of radioactive $^{132}\text{Sn}$ with $^{64}\text{Ni}$

J. F. Liang, D. Shapira, J. R. Beene, C. J. Gross, R. L. Varner, A. Galindo-Uribarri,  
J. Gomez del Campo, P. A. Hausladen, P. E. Mueller, D. W. Stracener  
*Physics Division, Oak Ridge National Laboratory, Oak Ridge, Tennessee 37831*

H. Amro, J. J. Kolata  
*Department of Physics, University of Notre Dame, Notre Dame, IN 46556*

J. D. Bierman  
*Physics Department AD-51, Gonzaga University, Spokane, Washington 99258-0051*

A. L. Caraley  
*Department of Physics, State University of New York at Oswego, Oswego, NY 13126*

K. L. Jones  
*Department of Physics and Astronomy, Rutgers University, Piscataway, NJ 08854*

Y. Larochelle  
*Department of Physics and Astronomy, University of Tennessee, Knoxville, Tennessee 37966*

W. Loveland, D. Peterson  
*Department of Chemistry, Oregon State University, Corvallis, Oregon 97331*  
(Dated: October 28, 2018)

Evaporation residue and fission cross sections of radioactive  $^{132}\text{Sn}$  on  $^{64}\text{Ni}$  were measured near the Coulomb barrier. A large sub-barrier fusion enhancement was observed. Coupled-channel calculations including inelastic excitation of the projectile and target, and neutron transfer are in good agreement with the measured fusion excitation function. When the change in nuclear size and shift in barrier height are accounted for, there is no extra fusion enhancement in  $^{132}\text{Sn}+^{64}\text{Ni}$  with respect to stable  $\text{Sn}+^{64}\text{Ni}$ . A systematic comparison of evaporation residue cross sections for the fusion of even  $^{112-124}\text{Sn}$  and  $^{132}\text{Sn}$  with  $^{64}\text{Ni}$  is presented.

PACS numbers: 25.60.-t, 25.60.Pj

## I. INTRODUCTION

Fusion of heavy ions has been a topic of interests for several decades[1]. One motivation is to understand the reaction mechanisms so that the production yield of heavy elements can be better estimated by model calculations. The formation of a compound nucleus is a complex process. The projectile and target have to be captured inside the Coulomb barrier and subsequently evolve into a compact shape. In heavy systems, the dinuclear system can separate during shape equilibration prior to passing the saddle point. This quasifission process is considered the primary cause of fusion hindrance[2, 3, 4].

At energies near and below the Coulomb barrier, the structure of the participants plays an important role in influencing the fusion cross section[5, 6, 7]. Sub-barrier fusion enhancement due to nuclear deformation and inelastic excitation has been observed[8, 9, 10, 11, 12]. Coupled-channel calculations have successfully reproduced experimental data by including nuclear deformation and inelastic excitation. Nucleon transfer is another important channel to be considered[13, 14].

Recently available radioactive ion beams offer the opportunity to study fusion under the influence of strong

nucleon transfer reactions. Several theoretical works have predicted large enhancement of sub-barrier fusion involving neutron-rich radioactive nuclei[15, 16, 17, 18, 19]. In addition, the compound nucleus produced in such reactions is predicted to have a higher survival probability and longer lifetimes. This is encouraging for super-heavy element research. If high-intensity, neutron-rich radioactive beams become available in the future, new neutron-rich heavy nuclei may be synthesized with enhanced yields. The longer lifetime of new isotopes of heavy elements would enable the study of their atomic and chemical properties[20]. However, the current intensity of the radioactive beams is several orders of magnitude lower than that of stable beams. It is thus not practical to use such beams for heavy element synthesis experiments, but they do provide excellent opportunities for studying reaction mechanisms of fusion involving neutron-rich radioactive nuclei.

Fusion enhancement, with respect to a one-dimensional barrier penetration model prediction, has been observed in experiments performed with neutron-rich radioactive ion beams at sub-barrier energies[21, 22, 23, 24, 25]. For instance, the effect of large neutron excess on fusion enhancement can be seen in  $^{29,31}\text{Al}+^{197}\text{Au}$ [23].

However, when comparing reactions involving stable isotopes of the projectile or target, the fusion excitation functions are very similar if the change in nuclear sizes is accounted for.

This paper reports results of fusion excitation functions measured with radioactive  $^{132}\text{Sn}$  on  $^{64}\text{Ni}$ . The doubly magic ( $Z=50$ ,  $N=82$ )  $^{132}\text{Sn}$  has eight neutrons more than the heaviest stable  $^{124}\text{Sn}$ . Its  $N/Z$  ratio (1.64) is larger than that of stable doubly magic nuclei  $^{48}\text{Ca}$  (1.4) and  $^{208}\text{Pb}$  (1.54) which are commonly used for heavy element production[26]. Evaporation residue (ER) and fission cross sections were measured. The sum of ER and fission cross sections are taken as the fusion cross section.

The experimental apparatus is described in Sect. II and data reduction procedures in Sect. III. The results and comparison with model calculations are presented in Sect. IV. In Sect. V a comparison of ER and fusion cross sections with those resulting from stable Sn isotopes on  $^{64}\text{Ni}$  is discussed. A summary is given in Sect. VI.

## II. EXPERIMENTAL METHODS

The experiment was carried out at the Holifield Radioactive Ion Beam Facility. A 42 MeV proton beam produced by the Oak Ridge Isochronous Cyclotron was used to bombard a uranium carbide target. The fission fragments were ionized by an electron beam plasma ion source. The largest yield of mass  $A=132$  fragments was  $^{132}\text{Te}$ . Therefore, it was necessary to suppress  $^{132}\text{Te}$ . This was accomplished by introducing sulfur into the ion source then selecting the mass 164  $\text{XS}^+$  molecular ions from the extracted beam. The  $^{132}\text{Te}$  to  $^{132}\text{Sn}$  ratio in the ion beam was found to be suppressed by a large factor ( $\sim 7 \times 10^4$ ) compared to that observed with the mass 132 atomic beam. The mass 164  $\text{SnS}^+$  beam was converted into a  $\text{Sn}^-$  beam by passing it through a Cs vapor cell where the molecular ion underwent breakup and charge exchange[27]. The negatively charged Sn was subsequently injected into the 25 MV electrostatic tandem accelerator to accelerate the beam to high energies. The measurement was performed at energies between 453 and 620 MeV. The average beam intensity was 50,000 particles per second (pps) with a maximum of 72,000 pps. The ER cross sections measured between 453 and 560 MeV have been reported previously[24].

The purity of the Sn beam was measured by an ionization chamber mounted at zero degrees. Figure 1 displays the energy loss spectra of a 560 MeV  $A=132$  beam with and without the sulfur purification. The dashed curves are the results of fitting the spectrum with Gaussian distributions to estimate the composition of the beam. In the upper panel, the beam is primarily  $^{132}\text{Te}$  without sulfur in the ion source. When sulfur was introduced in the ion source, the beam was 96%  $^{132}\text{Sn}$ , as shown in the lower panel. The small amount of Sb and Te had a negligible impact on the measurement because their atomic number is higher. Fusion of the target with these iso-

baric contaminants at sub-barrier energies should have been suppressed due to the higher Coulomb barriers.

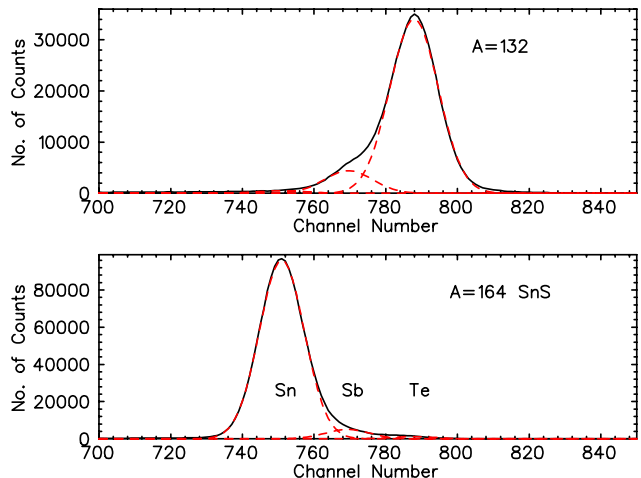


FIG. 1: (Color online) Composition of a 560 MeV mass  $A=132$  beam measured by the ionization chamber. Top panel: The mass  $A=132$  beam without purification where Te and Sb are the major components of the beam. Bottom panel: Sulfur was introduced into the target ion source and  $\text{SnS}$  was selected by the mass separator. The dashed curves are results of fitting the spectrum with three Gaussian distributions. The isobar contaminants  $^{132}\text{Sb}$  and  $^{132}\text{Te}$  were suppressed considerably.

The apparatus for the fusion measurement is shown in Fig. 2. A thick  $^{64}\text{Ni}$  target ( $1.0 \text{ mg/cm}^2$ ) was used to compensate for the low beam intensity. Since the compound nucleus decays by particle evaporation and fission, the evaporation residue (ER) and fission cross sections were measured. The ERs were detected by the ionization chamber at zero degrees and the fission fragments were detected by an annular double-sided silicon strip detector.



FIG. 2: (Color online) Apparatus for measuring fission and evaporation residues cross sections induced by low intensity beams in inverse kinematics.

The ERs were identified by the time-of-flight measured with the microchannel plate timing detector located in front of the ionization chamber and by energy loss in the ionization chamber. The two microchannel plate timing detectors located before the target were used to monitor the beam intensity and to provide the timing reference for the time-of-flight measurement. The microchannel plate timing detector in front of the ionization chamber was position sensitive and was used to monitor the beam position. It was located 200 mm from the target and had

a 25 mm diameter Mylar foil. The ionization chamber was filled with  $\text{CF}_4$  gas so that it could function at rates up to 50,000 pps. Higher beam intensities occurred in some of the fission measurements, requiring the ionization chamber to be turned off. The data acquisition was triggered by either the beam signal rate down scaled by a factor of 1000, the coincidence of the delayed beam signal and ER signal, or the silicon detector signal. A 350 MeV Au beam that resembled ERs was measured by the ionization chamber to calibrate the energy loss spectrum. The ER cross section was obtained by taking the ratio of the ER yield to the target thickness and the integrated beam particles in the ionization chamber. A detailed description of the ER measurement technique used in this experiment can be found in Ref. [28].

The annular double-sided silicon strip detector (Micron Semiconductor Design S2) was located 42 mm from the target. It had 48 concentric strips on one side and 16 pie-shaped sectors on the other side. The inner diameter was 35 mm and the outer diameter was 70 mm. The thickness of the detector was 300  $\mu\text{m}$ . The detection angles spanned 15.6° to 39.6°. The fission fragments were identified by requiring a coincidence of events in the Si detector and by the folding angle distributions of the detected particles.

### III. DATA REDUCTION PROCEDURES

#### A. Evaporation residues

Since this was an inverse kinematics reaction, the ERs recoiled in the forward direction in a narrow cone. The apparatus was designed to have high efficiency for detecting ERs. The efficiency of the apparatus was estimated by Monte Carlo simulations. The angular distribution of the ERs was generated by statistical model calculations using the code PACE2[29]. The input parameters for the statistical model calculations will be discussed later in this paper. The calculated efficiency for the lowest bombarding energy is  $93 \pm 1\%$ . It increases as the reaction energy increases and reaches  $98 \pm 1\%$  at the highest energy.

A relatively thick target was used in this experiment. The beam lost approximately 40 MeV after passing through the target (13 MeV in the center of mass). For this reason, the measured cross section is an average of the contributions from the beam interacting throughout the thickness of the target. The variation of ER cross sections is not very large at energies above the Coulomb barrier because the shape of the excitation function is almost flat. Therefore, the measured cross section is close to that would be measured at an energy corresponding to the middle of the target. However, at energies below the barrier the ER cross section falls off exponentially. The cross section near the entrance of the target has more weight than that near the exit. Smooth curves fitting the excitation function in this rapidly varying region were

used to determine the reaction energy associated with the measured cross section.

An iterative method was used to determine the effective reaction energy for the thick target measurement. First, the measured cross sections and the beam energies calculated at the middle of the target were fitted by a tensioned spline[30] where the smoothness of the curve could be adjusted. The resulting curve was then used to calculate the thick target cross section for each measurement, according to

$$\sigma_i = \int \frac{\sigma(E)}{dE/dx} dE/\rho$$

where  $\sigma(E)$  is the curve generated by the spline fit,  $dE/dx$  is the stopping power of  $^{132}\text{Sn}$  in  $^{64}\text{Ni}$ , and  $\rho$  is the target thickness. The integration limits were the energies of the beam at the exit of the target and at the entrance of the target. The energy,  $E_i$ , corresponding to the cross section,  $\sigma_i$ , was obtained by interpolation using the fitted curve. This set of energies was used as the input for the next iteration of the fit. The result converged very quickly. After five iterations, the energies differed from the previous iteration energies by less than 0.2 MeV. The validity of this method was checked by generating data from a known function such as the Wong formula [31] and folding in the effects of target thickness.

Comparing to the cross-section-weighted-average method described in Ref. [28], the differences in energies determined by these two methods are not noticeable at high energies because the excitation function is fairly flat. However, at energies below the barrier, the energy determined by the cross-section-weighted-average method is larger than that determined by the method described above and disagrees with the measurement in Ref. [32], as can be seen in Fig. 3. Furthermore, it is found that using data generated from a known function the effective energy obtained by the cross-section-weighted-average method is shifted to too high an energy in the exponential falloff region.

The uncertainty of the energy determination was estimated by comparison with the method using the cross section weighted average. The average uncertainty of the effective reaction energy is 2.3 MeV in the region where the excitation function is almost flat and increases to 3.9 MeV in the exponential fall off region. The uncertainty is larger, 5.8 MeV, for the lowest energy data point because an extrapolation is required for calculating the thick target cross section and the extrapolation region is influenced by the location of the next higher energy point.

To verify our measurement technique, the ER cross sections for  $^{124}\text{Sn}+^{64}\text{Ni}$  in inverse kinematics were measured and compared to those published by Freeman *et al.* measured with a thin target[32]. It is noted that some of our measurements were performed at energies different from those of Ref. [32]. The comparison is shown in Fig. 3. Our data (open triangles) are in good agreement with those measured by Freeman *et al.* [32] (filled stars).

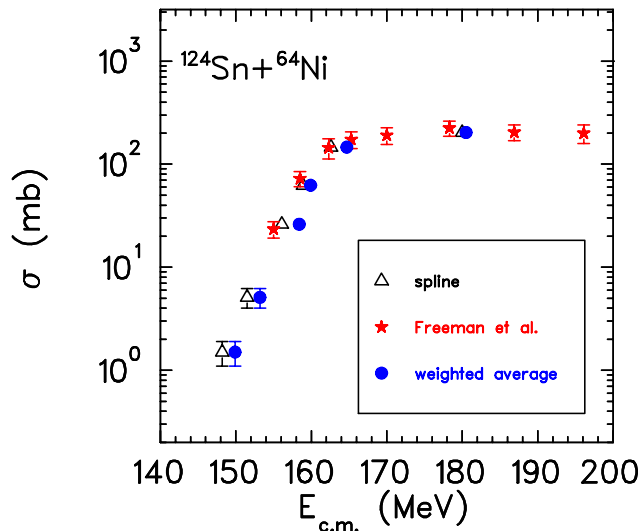


FIG. 3: (Color online) Comparison of ER cross sections for  $^{64}\text{Ni}+^{124}\text{Sn}$  measured in this work and by Freeman *et al.* [32] (filled stars). The filled circles are for energies determined by the method described in Ref. [28] and the open triangles are for energies determined by the method described in this paper.

The solid circles are for energy determined by the cross-section-weighted-average method described in Ref. [28].

## B. Fission

Fission fragments were identified by requiring a coincidence of two particles detected by the pie-shaped sectors of the Si strip detector on either side of the beam. Figure 4(a) and (b) present two-dimensional histograms of particle energy and strip number of the Si detector for coincident events taken from 560 MeV and 620 MeV  $^{132}\text{Sn}+^{64}\text{Ni}$ , respectively. They were compared to the kinematics calculation displayed in Fig. 4(c) and (d) where the fission fragments, elastically scattered Sn and Ni are shown by the solid, dash-dotted and dotted curves, respectively. The angular range of the Si strip detector is between the two vertical dashed lines. The elastically scattered Ni and Sn appear in the upper right hand corner and center of the histogram, respectively. The fission events are located in the gated area.

The folding angle distributions of the fragments were used to distinguish fission from other reactions, such as deep inelastic reactions. Since there are two solutions for the kinematics of the inverse reaction, as shown in Fig. 4(c) and (d), the fragment angular correlation is not as simple as that in normal kinematics. Monte Carlo simulations were performed to provide guidance. It was assumed that only fusion-fission results from a full momentum transfer. The width of the mass distribution was taken from the  $^{58}\text{Ni}+^{124}\text{Sn}$  measurement [33]. The width of the mass distribution was varied to estimate the uncer-

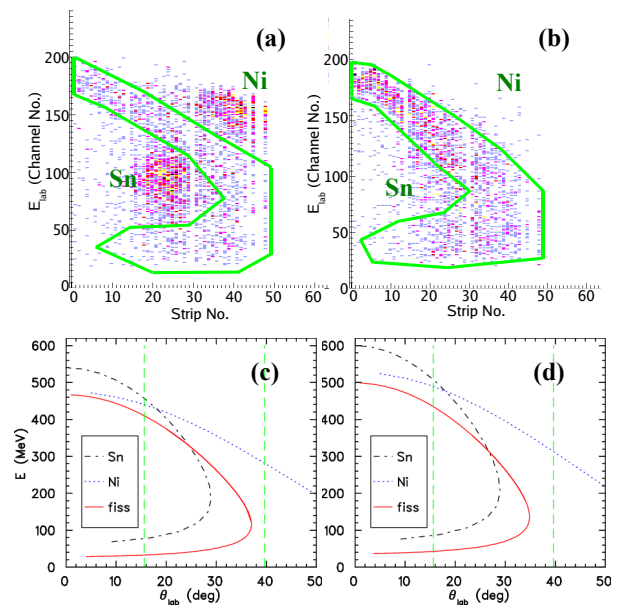


FIG. 4: (Color online) (a) and (b) Two dimensional histograms of energy and strip number for coincident events from 560 and 620 MeV  $^{132}\text{Sn}+^{64}\text{Ni}$ , respectively, measured by the annular double-sided silicon strip detector. The gated area shows events from fission and other reactions. (c) and (d) Kinematics of energy as a function of scattering angle for 560 and 620 MeV  $^{132}\text{Sn}+^{64}\text{Ni}$ , respectively, elastic scattering and fission fragments. The dash-dotted and dotted curves are for the elastically scattered Sn and Ni, respectively whereas the solid curve is for the fission fragments. The angular range of the Si strip detector is between the two vertical dashed lines.

tainty of the simulation. The transition state model [34] was used to predict the fission fragment angular distribution. In Fig. 5 the simulated fission fragment folding angle distributions for 550 MeV  $^{124}\text{Te}+^{64}\text{Ni}$  are compared with a stable beam test measurement. The folding angle distributions for one of the fragments detected in strip 2 ( $16.2^\circ$ ), strip 22 ( $27.7^\circ$ ), and strip 41 ( $36.8^\circ$ ) are shown. The gap in the spectra at strip 14, 30, 44, 46, and 47 are malfunctioning strips in the detector.

The Monte Carlo simulated folding angle distributions for fission are shown in the middle panels of Fig. 5 and compared to those of measurements shown in the left panels. For one of the fragments detected at forward angles, strip 2 for example, the predicted angular distribution of the other fragment is similar to that of the measurement. Most of these events are considered as resulting from fission. For one of the fragments detected near the middle part of the detector, strip 22 for instance, there are differences between measurement and simulation in the shapes of the angular distributions of the other fragment. It is predicted that the other fission fragment is distributed around strip 40. The measured distribution spreads to more forward angles. For one of the fragments detected at the backward angles, the yield of the other fragment is predicted to be small and they are equally

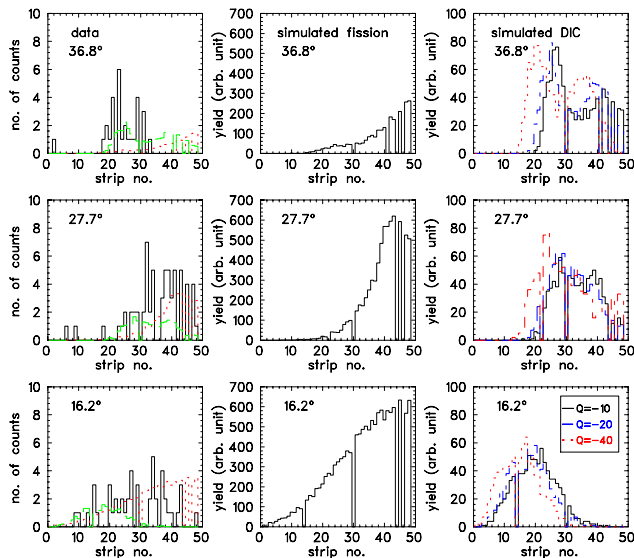


FIG. 5: (Color online) Left panels: Folding angle distributions for 550 MeV  $^{124}\text{Te}+^{64}\text{Ni}$  for one of the fragments detected at  $16.2^\circ$  (strip 2),  $27.7^\circ$  (strip 22), and  $36.8^\circ$  (strip 41) by the annular double-sided silicon strip detector. The elastic scattering events are excluded. The dotted and dashed histograms are the results of fitting the data with simulated fission and deep inelastic collisions with  $Q=-20$  MeV, respectively (see text). Middle panels: Results of Monte Carlo simulations for fission events. Right panels: Results of Monte Carlo simulations for deep inelastic scattering events. The solid curves are for reaction  $Q$  value of  $-10$  MeV, the dashed curves are for  $Q=-20$  MeV, and the dotted curves are for  $Q=-40$  MeV.

distributed between the middle part of the detector and the outer edge of the detector. But the measured events appear in the middle part of the detector. There are no events in the region where fission events are expected. These differences are attributed to the contribution from other reaction mechanisms, most likely deep inelastic collisions.

An attempt was made to simulate these deep inelastic collision events. It was assumed that the mass of these products were projectile- and target-like and the angular distribution at forward angles followed a  $1/\sin(\theta)$  dependence. The right panels of Fig. 5 show the results of simulations performed for reaction  $Q$  values of  $-10$  (solid),  $-20$  (dashed), and  $-40$  MeV (dotted). It can be seen that the overlap of fission and deep inelastic collisions becomes larger at more backward angles. At strip 41 ( $36.8^\circ$ ), deep inelastic collisions account for all the events.

The relative contribution of fission and deep inelastic collisions were obtained by fitting the simulated folding angle distributions to the measured distributions for all the detector strips using the CERN library program MINUIT[35]. In the fits, the normalization coefficients for the simulated distributions were the only two variable parameters. The results of the fits are shown in the left panels of Fig. 5 by the dotted and dashed histograms for fission and deep inelastic collisions with  $Q=-20$  MeV, re-

spectively. The number of fission events in the measured distributions were taken as the summed events in each strip multiplied by the relative contribution of fission.

The folding angle distributions for  $^{132}\text{Sn}+^{64}\text{Ni}$  are shown in Fig. 6. Due to the low statistics, it was not practical to extract the fission events by fitting the folding angle distributions. As an alternative, the fission events were extracted by setting gates on the folding angle distributions using the simulated distributions as references. This gating method was also tested with the  $^{124}\text{Te}+^{64}\text{Ni}$  measurement. The fission cross sections obtained by the fitting method and the gating method agreed within 10%.

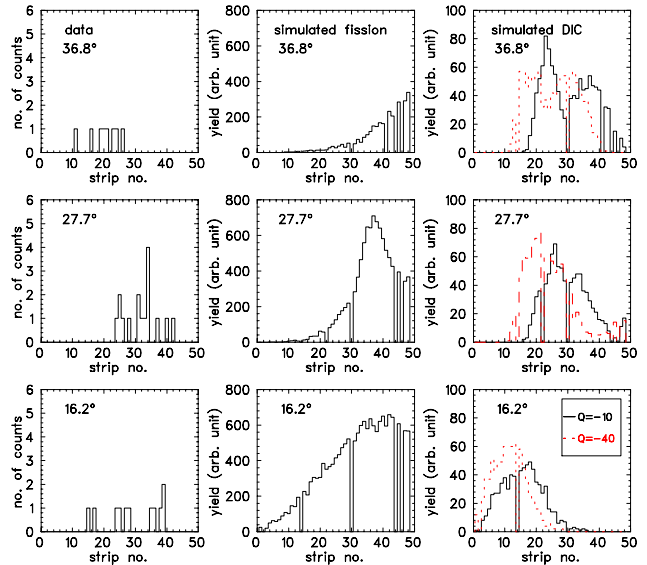


FIG. 6: (Color online) Left panels: Folding angle distributions for 560 MeV  $^{132}\text{Sn}+^{64}\text{Ni}$  for one of the fragments detected at  $16.2^\circ$  (strip 2),  $27.7^\circ$  (strip 22), and  $36.8^\circ$  (strip 41) by the annular double-sided silicon strip detector. The elastic scattering events are excluded. Middle panels: Results of Monte Carlo simulations for fission events. Right panels: Results of Monte Carlo simulations for deep inelastic scattering events. The solid curves are for reaction  $Q$  value of  $-10$  MeV, and the dotted curves are for  $Q=-40$  MeV.

The Monte Carlo simulation was also employed to calculate the coincidence efficiency of the detector. The efficiency increased from  $5.7\pm 0.9\%$  at 530 MeV to  $7.6\pm 0.8\%$  at 620 MeV bombarding energy.

In the present work, the dynamic range of the amplifiers was not sufficiently large resulting in the distortion of the high energy signals. In the future, new amplifiers that are more suitable for measuring the energy of fission fragments will be used so that the mass ratio of reaction products can be obtained to help distinguish fission events from other reaction channels.

The formation of a compound nucleus depends on whether the interacting nuclei are captured inside the fusion barrier and whether the dinuclear system can subsequently evolve into a compact shape. Quasifission occurs when the dinuclear system fails to cross the saddle

level density parameter (a)	$A/8 \text{ MeV}^{-1}$
$a_f/a_n$	1.04
diffuseness of spin distribution ( $\Delta l$ )	$4 \hbar$
fission barrier	Sierk[45]

TABLE I: Input parameters for statistical model calculations.

point to reach shape equilibrium. Since the beam intensity was several orders of magnitude lower than that of stable beams and the reaction was in inverse kinematics, making separation of fusion-fission and quasifission very difficult, there was no attempt to distinguish quasifission from fusion-fission in this work. Furthermore, the experimental results are compared to barrier penetration models which describe the capture process, making it unnecessary to separate these two processes.

#### IV. COMPARISON WITH MODEL CALCULATIONS

##### A. Statistical model

The compound nucleus formed in  $^{132}\text{Sn}+^{64}\text{Ni}$  decays by particle evaporation and fission. Statistical models have successfully described compound nucleus decay for a wide range of fusion reactions. The measured ER and fission cross sections are compared with the predictions of the statistical model code PACE2[29]. The input parameters were obtained by simultaneously fitting the data from stable Sn on  $^{64}\text{Ni}$ [32, 36] and the measured fusion cross sections[36] were used for the calculations. Figure 7(a), (b), and (c) displays the comparison of calculations and data for  $^{112,118,124}\text{Sn}+^{64}\text{Ni}$ , respectively. The calculations reproduce the measurements well except for the ER cross sections of  $^{112}\text{Sn}+^{64}\text{Ni}$ . Table I lists the input parameters for the calculations. Without adjusting the parameters, calculations for  $^{132}\text{Sn}+^{64}\text{Ni}$  were performed. The results are shown in Fig. 7(d). Very good agreement between the calculation and the data can be seen.

It is noted that some of the parameters used in our calculations are different from those used by Lesko *et al.* [36]. In their calculations, the code CASCADE[37] was used. The mass of the nuclei in the decay chain was calculated using the Myers droplet model[38]. The diffuseness of the spin distribution was  $\Delta l = 15\hbar$  and the ratio of level density at the saddle point to the ground state,  $a_f/a_n$ , was set to 1.0. In this work, a compilation of measured masses[39],  $\Delta l = 4\hbar$ , and  $a_f/a_n = 1.04$  were used.

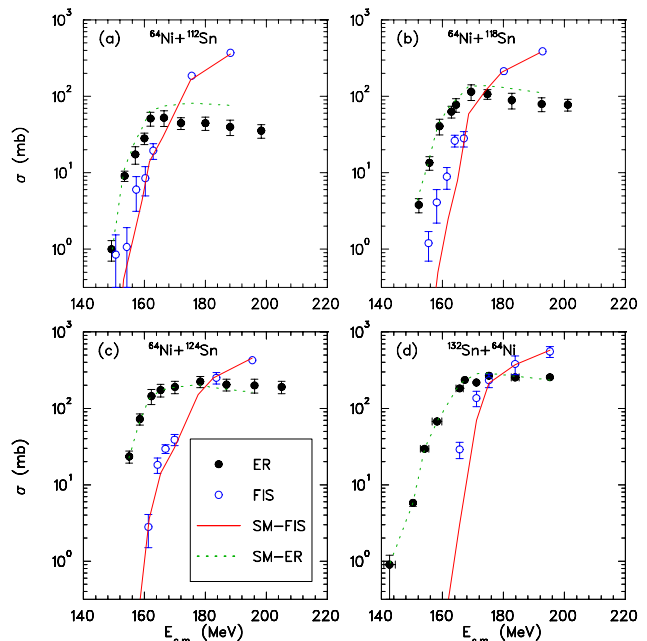


FIG. 7: (Color online) Comparison of measured ER (filled circles) and fission (open circles) cross sections with statistical model calculations. The solid and the dotted curves are the calculated fission and ER cross sections, respectively, using the measured fusion cross sections as input. (a)  $^{64}\text{Ni}+^{112}\text{Sn}$ , (b)  $^{64}\text{Ni}+^{118}\text{Sn}$ , (c)  $^{64}\text{Ni}+^{124}\text{Sn}$  (Freeman *et al.*[32]), and (d)  $^{132}\text{Sn}+^{64}\text{Ni}$  (this work)

##### B. Coupled-channel calculation

In general, sub-barrier fusion enhancement can be described by coupled-channel calculations. The fusion cross section of  $^{132}\text{Sn}+^{64}\text{Ni}$ , the sum of ER and fission cross sections, is compared with coupled-channel calculations using the code CCFULL[40]. The interaction potential ( $V_o=82.46 \text{ MeV}$ ,  $r_o=1.18 \text{ fm}$ , and  $a=0.691 \text{ fm}$ ) was taken from the systematics of Broglia and Winther[41]. The result of the calculations are compared with the data in Fig. 8. The dotted curve is the prediction of a one-dimensional barrier penetration model and it can be seen that it substantially underpredicts the sub-barrier cross sections. The coupled-channel calculation including inelastic excitation of  $^{64}\text{Ni}$  to the first  $2^+$  and  $3^-$  states and  $^{132}\text{Sn}$  to the first  $2^+$  state is shown by the dashed curve. The transition matrix elements,  $B(E\lambda)$ , of  $^{64}\text{Ni}$  were obtained from Ref. [42, 43] and the  $B(E2)$  of  $^{132}\text{Sn}$  was obtained from a recent measurement by Varner *et al.*[44]. This calculation overpredicts the data at energies near the barrier and underpredicts the data well below the barrier.

The neutron transfer reactions have positive Q values for transferring two to six neutrons from  $^{132}\text{Sn}$  to  $^{64}\text{Ni}$ . Since there is no neutron transfer data available for this reaction, the transfer coupling form factor is unknown. Thus, the coupled-channel calculation including transfer and inelastic excitation was performed with one effec-

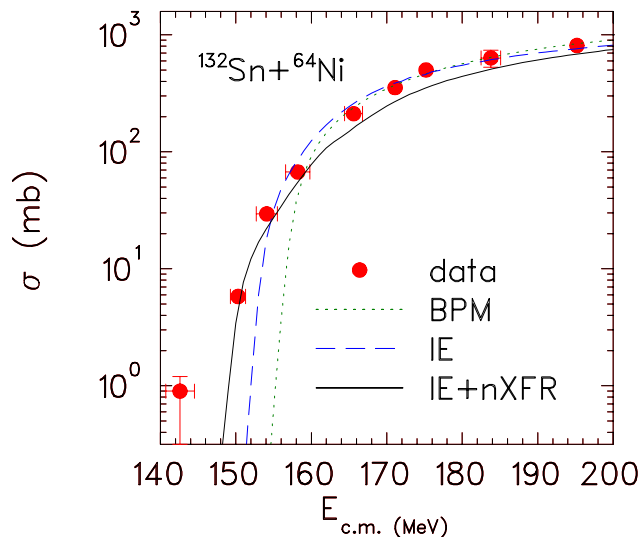


FIG. 8: (Color online) Comparison of  $^{132}\text{Sn}+^{64}\text{Ni}$  fusion data (filled circles) with a one-dimensional barrier penetration model calculation (dotted curve). The coupled-channel calculation including inelastic excitation of the projectile and target is shown by the dashed curve and the calculation including inelastic excitation and neutron transfer is shown by the solid curve.

tive transfer channel using the Q value for two-neutron transfer. The coupling constant was adjusted to fit the data. The calculation with the coupling constant set to 0.48 is shown by the solid curve. It reproduces the data very well except for the lowest energy data point which has large uncertainties in energy and in cross section. A better treatment of the transfer channels based on experimental transfer data would help improve understanding of the influence of transfer on fusion. Experimental neutron transfer data on  $^{132}\text{Sn}+^{64}\text{Ni}$  in the future would be very useful.

## V. DISCUSSION

The ER cross section can be described by

$$\sigma_{ER} = \pi\lambda^2 \sum_{l=0}^{l_c} (2l+1)\sigma_l,$$

where  $\lambda$  is the de Broglie wave length,  $l_c$  the maximum angular momentum for ER formation and  $\sigma_l$  the partial cross section. The reduced ER cross sections for  $^{64}\text{Ni}$  on stable-even Sn isotopes[32] are compared with that for  $^{132}\text{Sn}+^{64}\text{Ni}$  in Fig. 9. The reduced ER cross section is defined as the ER cross section divided by the kinematic factor  $\pi\lambda^2$ . It can be seen that the ER cross sections saturate at high energies as fission becomes a significant fraction of the fusion cross section. In addition, the saturation value increases as the neutron excess in Sn increases. This is consistent with the fact that the

fission barrier height increases for the more neutron-rich compound nuclei.

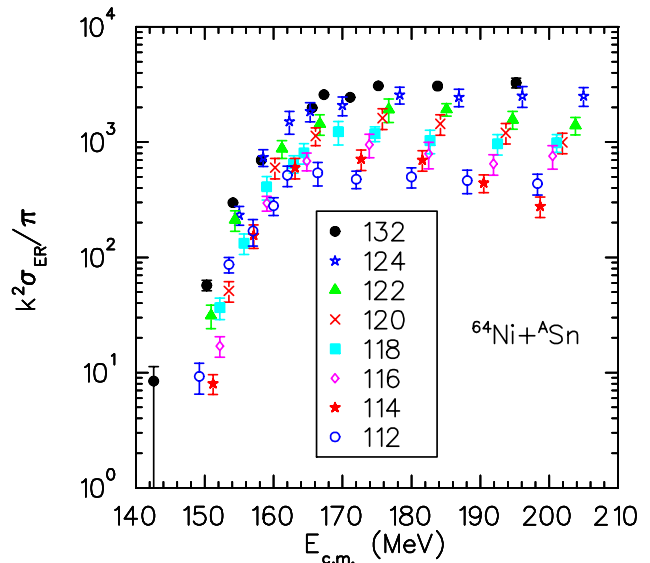


FIG. 9: (Color online) The reduced ER cross section as a function of the center of mass energy for  $^{64}\text{Ni}$  on stable even Sn isotopes[32] and radioactive  $^{132}\text{Sn}$ .

In Fig. 10, the measured reduced ER cross sections for Ni+Sn as a function of the calculated average mass of the ERs, predicted by PACE2, are presented. In the same reaction, the higher mass ERs are produced at lower beam energies because of the lower excitation energies of the compound nucleus. As the neutron excess in the compound nucleus increases, neutron evaporation becomes the dominant decay channel. The PACE2 calculation predicts that a compound nucleus made with Sn isotopes of mass number greater than 120 decays essentially 100% by neutron evaporation and Pt isotopes are the primary ERs. The mass of the compound nucleus is different when it is produced with different Sn isotopes. However, it can be seen that Pt of a particular mass can be produced with different Sn isotopes if different numbers of neutrons are evaporated. The reaction with a more neutron-rich Sn produces the same Pt isotope at a higher rate. With  $^{132}\text{Sn}$  as the projectile, the ERs are so neutron-rich that they cannot be produced by stable Sn induced reactions. This suggests that it may be beneficial to use neutron-rich radioactive ion beams to produce new isotopes of heavy elements.

The fusion excitation functions of  $^{64}\text{Ni}$  on stable even Sn isotopes[36] are compared with that of  $^{132}\text{Sn}+^{64}\text{Ni}$  in Fig. 11. In order to remove the effects of the difference in nuclear sizes, the cross section is divided by  $\pi R^2$  with  $R=1.2(A_p^{1/3}+A_t^{1/3})$  fm, where  $A_p$  ( $A_t$ ) is the mass number of the projectile (target). The reaction energy in the center of mass is divided by the barrier height predicted by the Bass model[46]. It can be seen that the fusion of  $^{132}\text{Sn}$  and  $^{64}\text{Ni}$  is not enhanced with respect to the stable-even Sn isotopes when the difference in nuclear sizes is

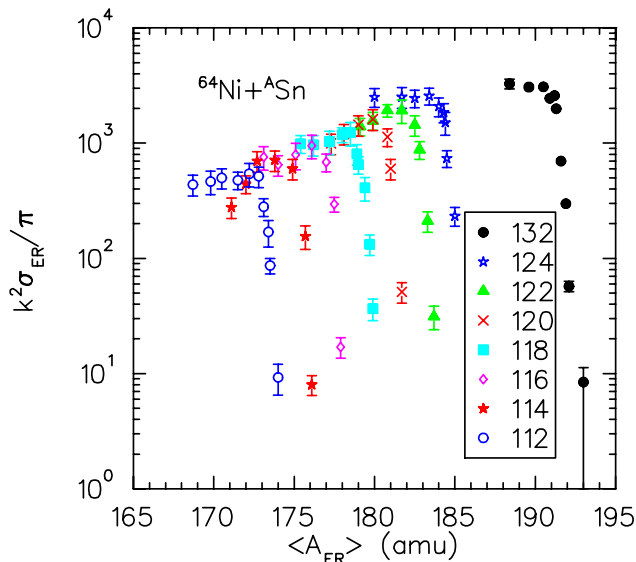


FIG. 10: (Color online) The reduced ER cross section as a function of the calculated average mass of ERs predicted by PACE2[29] for  $^{64}\text{Ni}$  on stable even Sn isotopes[36] and radioactive  $^{132}\text{Sn}$ .

considered.

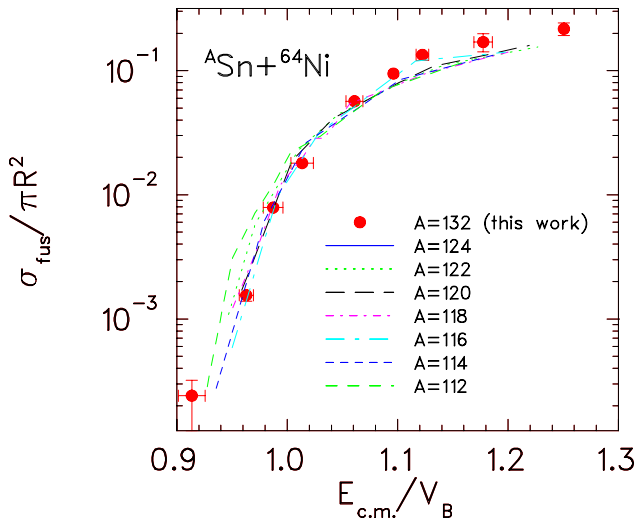


FIG. 11: (Color online) Comparison of fusion excitation functions for  $^{64}\text{Ni}$  on stable even Sn isotopes[36] and radioactive  $^{132}\text{Sn}$ . The change in nuclear sizes are corrected by factoring out the area and the Bass barrier height[46] in the cross section and energy, respectively.

The lowest energy data point has large uncertainties. The cross section seems enhanced comparing to the stable beam measurements in Fig. 9 and Fig. 11. A more pronounced enhancement appears when the data point is compared to our coupled-channel calculations (Fig. 8) and to a time-dependent Hartree-Fock calculation[47]. To further explore if fusion is enhanced at this low energy region, we plan to repeat the measurement with an im-

proved apparatus where the thickness of the Mylar foil in the microchannel plate timing detector located in front of the ionization chamber will be reduced. This will allow a better separation of the energy loss signals from ERs and scattered beams in the ionization chamber at low bombarding energies.

The Q values for transferring two to six neutrons from  $^{132}\text{Sn}$  to  $^{64}\text{Ni}$  are positive. It is necessary to include neutron transfer in coupled-channel calculations to reproduce experimental results. As the neutron excess in the Ni isotopes decreases, the number of neutron transfer channels with positive Q values increases for  $^{132}\text{Sn}+\text{Ni}$ . In  $^{132}\text{Sn}+^{58}\text{Ni}$ , the Q values for transferring one to sixteen neutrons from  $^{132}\text{Sn}$  to  $^{58}\text{Ni}$  are positive and range from 1.7 to 17.4 MeV. A large sub-barrier fusion enhancement due to the coupling to neutron transfer is expected to occur in  $^{132}\text{Sn}+^{58}\text{Ni}$ . An experiment to measure the fusion excitation function of  $^{132}\text{Sn}$  on  $^{58}\text{Ni}$  is in preparation.

Although  $^{132}\text{Sn}$  is unstable, its neutron separation energy is 7.3 MeV. This is not very low compared to stable nuclei. The sub-barrier fusion enhancement observed in  $^{132}\text{Sn}+^{64}\text{Ni}$  with respect to stable Sn nuclei can be accounted for by the change in nuclear sizes. No extra enhancement was found. However, an increased ER yield at energies above the barrier was observed as compared to stable Sn. As the shell closure is crossed, the binding energy for  $^{133}\text{Sn}$  decreases by a factor of two. The nuclear surface of  $^{133}\text{Sn}$  and even more neutron-rich Sn may be more diffused. The number of neutron transfer channels with positive Q values increases by a factor of two or more. Larger sub-barrier fusion enhancement beyond the nuclear size effect may be expected.

## VI. SUMMARY

Neutron-rich radioactive  $^{132}\text{Sn}$  beams were incident on a  $^{64}\text{Ni}$  target to measure fusion cross sections near the Coulomb barrier. With an average intensity of  $5 \times 10^4$  pps beams and a high efficiency apparatus for ER detection, the uncertainty of the measured ER cross section is small and comparable to that achieved in stable beam experiments. The efficiency for fission fragment detection was low but the detector had a very fine granularity. By requiring a coincident detection of the fission fragments and performing folding angle distribution analysis, fission events were identified. The excitation functions of ER and fission can be described by statistical model calculations using parameters that simultaneously fit the stable even Sn isotopes on  $^{64}\text{Ni}$  fusion data. A large sub-barrier fusion enhancement with respect to a one-dimensional barrier penetration model prediction was observed. The enhancement is attributed to the coupling of the projectile and target inelastic excitation and neutron transfer. The reduced ER cross sections at energies above the barrier are larger for the  $^{132}\text{Sn}$  induced reaction than those induced by stable Sn nuclei, as expected from the higher

fission barrier of the more neutron-rich compound nucleus. For a specific mass of ER, reactions with a more neutron-rich Sn have higher cross sections. When the fusion excitation functions are compared on a reduced scale, where the effects of nuclear size and barrier height are factored out, no extra fusion enhancement is observed in  $^{132}\text{Sn}+^{64}\text{Ni}$  with respect to stable Sn induced fusion. The fusion cross section measured at the lowest energy seems to be enhanced. Experiments to investigate this with an improved apparatus is planned.

## VII. ACKNOWLEDGMENT

We would like to thank D. J. Hinde for helpful and stimulating discussions. We wish to thank the HRIBF

staff for providing excellent radioactive beams and technical support. Research at the Oak Ridge National Laboratory is supported by the U.S. Department of Energy under contract DE-AC05-00OR22725 with UT-Battelle, LLC. W.L. and D.P. are supported by the the U.S. Department of Energy under grant no. DE-FG06-97ER41026.

- 
- [1] W. Reisdorf, J. Phys. G **20**, 1297 (1994).
  - [2] B. B. Back, Phys. Rev. C **31**, 2104 (1985).
  - [3] J. Töke *et al.*, Nucl. Phys. **A440**, 327 (1985).
  - [4] D. J. Hinde and M. Dasgupta, Phys. Lett. B **622**, 23 (2005).
  - [5] M. Beckerman, Rep. Prog. Phys. **51**, 1047 (1988).
  - [6] M. Dasgupta, D. J. Hinde, N. Rowley, and A. M. Stefanini, Annu. Rev. Nucl. Part. Sci. **48**, 401 (1998).
  - [7] A. B. Balantekin and N. Takigawa, Rev. Mod. Phys. **70**, 77 (1998).
  - [8] J. R. Leigh *et al.*, Phys. Rev. C **52**, 3151 (1995).
  - [9] J. D. Bierman, P. Chan, J. F. Liang, M. P. Kelly, A. A. Sonzogni, and R. Vandenbosch, Phys. Rev. Lett. **76**, 1587 (1996); Phys. Rev. C **54**, 3068 (1996).
  - [10] C. R. Morton *et al.*, Phys. Rev. Lett. **72**, 4074 (1994).
  - [11] A. M. Stefanini *et al.*, Phys. Rev. Lett. **74**, 864 (1995).
  - [12] A. A. Sonzogni, J. D. Bierman, M. P. Kelly, J. P. Lestone, J. F. Liang, and R. Vandenbosch, Phys. Rev. C **57**, 722 (1998).
  - [13] A. M. Stefanini, D. Ackermann, L. Corradi, J. H. He, G. Montagnoli, S. Beghini, F. Scarlassara, and G. F. Segato, Phys. Rev. C **52**, R1727 (1995).
  - [14] H. Timmers *et al.*, Nucl. Phys. **A633**, 421 (1998).
  - [15] N. Takigawa, H. Sagawa, and T. Shinozuka, Nucl. Phys. **A538**, 221c (1992).
  - [16] M. S. Hussein, Nucl. Phys. **A531**, 192 (1991).
  - [17] C. H. Dasso and R. Donangelo, Phys. Lett. B **276**, 1 (1992).
  - [18] V. Yu. Denisov, Eur. Phys. J. A **7** 87 (2000).
  - [19] V. I. Zagrebaev, Phys. Rev. C **67**, 061601(R) (2003).
  - [20] S. Hofmann, Prog. Part. Nucl. Phys. **46**, 293 (2001).
  - [21] K. E. Zyromski *et al.*, Phys. Rev. C **55**, R562 (1997).
  - [22] J. J. Kolata *et al.*, Phys. Rev. Lett. **81**, 4580 (1998).
  - [23] Y. X. Watanabe *et al.*, Eur. Phys. J. A **10**, 373 (2001).
  - [24] J. F. Liang *et al.*, Phys. Rev. Lett. **91**, 152701 (2003); Phys. Rev. Lett. **96**, 029903(E) (2006).
  - [25] J. F. Liang and C. Signorini, Int. J. Mod. Phys. E **14**, 1121 (2005).
  - [26] S. Hofmann and G. Münzenberg, Rev. Mod. Phys. **72**, 733 (2000).
  - [27] D. W. Stracener, Nucl. Instrum. and Methods B **204**, 42 (2003).
  - [28] D. Shapira *et al.*, Nucl. Instrum. and Methods A **551**, 330 (2005).
  - [29] A. Gavron, Phys. Rev. C **21**, 230 (1980).
  - [30] <http://www.netlib.org/fitpack/>.
  - [31] C. Y. Wong, Phys. Rev. Lett. **31**, 766 (1973).
  - [32] W. S. Freeman *et al.*, Phys. Rev. Lett. **50**, 1563 (1983).
  - [33] F. L. H. Wolfs, Phys. Rev. C **36**, 1379 (1987).
  - [34] R. Vandenbosch and J. R. Huizenga, *Nuclear Fission*, Academic Press, New York, (1973).
  - [35] F. James, *MINUIT reference manual (Version 94.1)*, Program Library D506, CERN, (1998).
  - [36] K. T. Lesko *et al.*, Phys. Rev. C **34**, 2155 (1986).
  - [37] F. Pühlhofer, Nucl. Phys. **A280**, 267 (1977).
  - [38] W. D. Myers, *Droplet Model of the Atomic Nucleus* (IFI/Plenum, New York, 1977).
  - [39] A. H. Wapstra, G. Audi, and C. Thibault, Nucl. Phys. **A729**, 129 (2003).
  - [40] K. Hagino, N. Rowley, and A. T. Kruppa, Compu. Phys. Commun. **123**, 143 (1999).
  - [41] R. A. Broglia and A. Winther, *Heavy Ion Reactions*, Addison-Wesley, (1991).
  - [42] S. Raman *et al.*, At. Data Nucl. Tables **36**, 1 (1987).
  - [43] R. H. Spear, At. Data Nucl. Tables **42**, 55 (1989).
  - [44] R. L. Varner *et al.*, Eur. Phys. J. A **25**, s01, 391 (2005).
  - [45] A. J. Sierk, Phys. Rev. C **33**, 2039 (1986).
  - [46] R. Bass, Nucl. Phys. **A231**, 45 (1974).
  - [47] A. S. Umar and V. E. Oberacker, Phys. Rev. C **74**, 061601(R) (2006).